Evaluation of Voronoi Meshes for Large Eddy Simulations of High Lift Aerodynamics

Emre Sozer*, Aditya S. Ghate†, Gaetan K. Kenway‡, Michael F. Barad§, Victor C.B. Sousa¶ and Cetin C. Kiris‖
NASA Ames Research Center, Moffett Field, CA, 94035

Numerical sensitivity to 3 different Voronoi seeding methods is investigated for Large Eddy Simulations (LES). A second order accurate, non-dissipative finite volume discretization is used to systematically investigate the effects of different polyhedral Voronoi mesh types using a sequence of three canonical problems with increasing complexity. First, inviscid isentropic vortex propagation is studied to demonstrate the substantial reduction of errors for rhombic dodecahedron and truncated octahedral cell types over Cartesian hexagonal cells of identical spacing. Furthermore, the reduction of errors induced at cell-size transitions (grid-coarsening interfaces) due to Lloyd smoothing iterations is quantified. It is shown that by utilizing an appropriate viscous flux discretization, a constant coefficient subgrid scale model is sufficient for non-linear stability at the 2:1 cell-size transitions on polyhedral grids, although some further error reduction does occur when smoothing is utilized. Next, forced homogeneous isotropic turbulence at an asymptotically large Reynolds number is studied to demonstrate the non-dissipative character of the inviscid flux discretization, and the non-linear robustness and accuracy offered by the viscous flux discretization using a subgrid scale model for all three Voronoi grid types. Finally, Wall-Modeled Large Eddy Simulations (WMLES) are performed to study the high-lift aerodynamics on the McDonnell Douglas 30P30N multi-element airfoil at two distinct grid levels and for two distinct Voronoi cell types. The formulation is shown to predict the aerodynamic loading with high accuracy at all angles of attack when sufficient resolution is reached, and the hexagonal prism grid topology, while computationally more expensive, has higher effective resolution compared to the Cartesian grid topology with the same spacing"

I. Introduction

Powered by the remarkable growth in High-Performance Computing (HPC) over the past 5-10 years, Large Eddy Simulations (LES) are increasingly becoming mainstream in academia as well as in industry. In aeronautics, this move towards LES is primarily due to its success in addressing major challenges faced by more traditional methods such as Reynolds Averaged Navier-Stokes (RANS) in predicting flows with strongly shear-dominant phenomena (such as jets), and non-equilibrium boundary layer flows (such as separated wall-bounded flows). Recent work has demonstrated superiority of LES in terms of accuracy over RANS in a wide range of flows of relevance to aircraft aerodynamics: a) High-lift flow-conditions near take-off and landing (referred to as $C_{L,max}$ prediction)[1–6], b) Shock-induced flow-separation leading to buffet at transonic conditions when perturbed about the cruise state[7], and c) Wing-body juncture flows that experience a corner-flow separation phenomenon that is particularly challenging for RANS closures[8–10]. This trend is consistent with the widespread interest in Wall-Modelled Large Eddy Simulations (WMLES) at the recent AIAA 4th High Lift Prediction Workshop (2022)[11] - a total of nine participants contributed WMLES submissions to HLPW4 while none of the participants at HLPW3 had performed WMLES. Of the 9 participants at HLPW4, 6 participants used unstructured grid topologies with either finite volume or finite element discretizations[12]. This is in stark contrast with the most academic research on WMLES technology which focuses on canonical benchmark problems, primarily relying on either finite difference discretizations on structured grids, or finite volume discretizations on hex-dominant unstructured grids (see reviews by Larsson et al.[13] and Park & Bose[14]).

Unstructured grids offer some advantages over structured curvilinear and Cartesian octree (using immersed boundary treatment) topologies: a) Highly automated and scalable body-conforming grid generation, b) Lack of coarse-fine cell

*Computational Aerosciences Branch, AIAA Member, emre.sozer@nasa.gov
†Science and Technology Corporation, AIAA Member, aditya.s.ghate@nasa.gov
‡Science and Technology Corporation, AIAA Member, gaetan.k.kenway@nasa.gov
§Computational Aerosciences Branch, AIAA Member, michael.f.barad@nasa.gov
¶Science and Technology Corporation, AIAA Member, victor.decarvalhobrittosousa@nasa.gov
‖Computational Aerosciences Branch, AIAA Senior Member, cetin.c.kiris@nasa.gov

volume jumps (or numerical impedence) in the grid due to utilization of smoothing methods, and c) Body-conforming off-body coarsening outside regions of resolvable vorticity. While finite difference methods can be extended to high orders of accuracy for a very low computational overhead compared to finite element or finite volume methods, the importance of reducing dissipation errors over dispersion errors in high Reynolds number LES is increasingly accepted across the community[15]. As such, second order non-dissipative finite volume discretizations are highly suitable for most LES for computational aerodynamics. Utilization of arbitrary polyhedral cell types has added advantages over hexahedral cells in terms of improved rotational invariance, which is particularly advantageous when predicting isotropic wave phenomena such as acoustics[15–18]. Furthermore, work done at the Center for Turbulence Research (CTR) at Stanford University has made a strong case for utilization of a specific form of Voronoi polyhedral grid type[19, 20]. Voronoi grids have several distinct advantages for LES: 1) Inherent high-quality of the cells generated by seeding the domain with regular point distributions allows utilization of robust and accurate, non-dissipative flux discretizations, 2) Isotropy of the resulting cells for arbitrarily complex geometries, along with the ability to tightly control the minimum cell size, allow use of efficient explicit time-differencing schemes, and 3) Grid-generation algorithms are highly scalable. As outlined in subsequent sections of this paper, the Voronoi meshing approach offers the choice of various possible cell types that can satisfy the aforementioned properties. The primary goals of this work are:

1) Comparative assessment of 3 distinct Voronoi grid types in terms of accuracy. This is done by studying the isentropic vortex propagation problem to observe the differences in dispersion errors seen on the three grid types. Furthermore, we also study the forced homogeneous isotropic turbulence test case to verify the non-dissipative character of the inviscid flux formulation and the dissipation enforced by a constant coefficient subgrid scale model.
2) Numerical treatment and implications of mesh smoothing across coarse-fine level changes. Aggressive grid coarsening can cause numerical instabilities as well as spurious numerical reflections[21–24]. One way to circumvent this issue is to use smoothing techniques (such as Lloyd smoothing [25]) in order to regularize the impedance jump. However, excessive smoothing also leads to a growth in the number of cells that lack the centroidality property. As such, there is a trade-off that needs to be investigated along with the role of the subgrid scale closure in dissipating any spurious modes that result at coarsening interfaces. The isentropic vortex propagation problem is used to study these complex interactions in detail.
3) Accuracy for $C_{L,max}$ prediction. Ultimately, the purpose of this paper is to investigate the accuracy of the unstructured grid WMLES formulation for computational aerodynamics. We study the McDonnell Douglas 30P30N multi-element airfoil geometry using two grid levels and two distinct Voronoi grid types.

The Launch, Ascent and Vehicle Aerodynamics (LAVA) computational framework[26] is used throughout this work, including for mesh generation. The remainder of this paper is outlined as follows. We begin by describing the numerical scheme proposed for the LES studies in Section II, followed by a discussion of different Voronoi mesh types and inherent properties of Voronoi meshes in Section III. In Section IV, the results for the three test problems investigated are presented and summarizing remarks are made in Section V.

II. Numerical Scheme

Navier-Stokes equations are solved using a 2nd order finite volume formulation which can be discretely expressed per control volume (computational cell) as:

$$J\frac{\Delta Q}{\Delta t} = \frac{1}{V}\sum_{f=1}^{N_f}\left(-F_c(Q_L, Q_R) + F_D(Q_f, \nabla Q_f)\right)A_f \tag{1}$$

where $Q = (p, u, v, w, T)$ is the primitive variable vector, $J = \partial W/\partial Q$ is the conservative to primitive transformation Jacobian with $W = (\rho, \rho u, \rho v, \rho w, E)$ as the conservative variable vector, V is the volume of the cell, N_f is the number of faces. The summation is carried out over the cell faces which are denoted by f, while L and R denote the states to the left and right of the face, respectively, as shown in Figure 1.

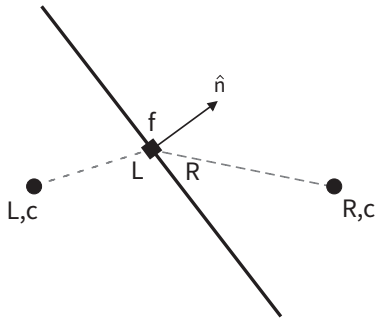

Fig. 1 Cell interface stencil notation.

A. Convective Flux

Convective fluxes at each face are evaluated via MUSCL [27] reconstructed primitive variable vectors from either side of the face as:

$$\begin{aligned} Q_L &= Q_{L,c} + \phi_L \nabla Q_{L,c} \cdot \vec{r}_L \\ Q_R &= Q_{R,c} + \phi_R \nabla Q_{R,c} \cdot \vec{r}_R \end{aligned} \tag{2}$$

where

$$\begin{aligned} \vec{r}_L &= \vec{x}_f - \vec{x}_{L,c} \\ \vec{r}_R &= \vec{x}_f - \vec{x}_{R,c} \end{aligned} \tag{3}$$

and $\nabla Q_{L,c}$ and $\nabla Q_{R,c}$ are, respectively, gradients at the left and right cell centroids calculated via the Green-Gauss method as described in Sozer et al. [28]. ϕ_L and ϕ_R are slope limiters evaluated for left and right reconstructions, with $\phi = 1$ representing no limiting and $\phi = 0$ representing first order evaluation. Limiting is typically not needed for subsonic flows and only becomes necessary in regions with flow discontinuities or with exceptionally bad cell quality affecting the gradient stencil. When a limiter is needed, a minmod [29] type function is used.

In the case of pure upwinding, Q_L and Q_R obtained via Eq. 2 are directly used to evaluate the convective flux through the face using AUSMPW+ [30] flux function.

For LES, however, the dissipative errors due to upwinding are known to be particularly unsuitable (compared to dispersion errors)[31] and we employ primitive variable blending at the face to obtain a central scheme as:

$$\begin{aligned} Q_C &= \frac{1}{2}\left(Q_L + Q_R\right) \\ \alpha &= \max\left(\zeta, 1 - \min(\phi_L, \phi_R)\right) \\ \overline{Q}_L &= (1-\alpha)Q_C + \alpha Q_L \\ \overline{Q}_R &= (1-\alpha)Q_C + \alpha Q_R \end{aligned} \tag{4}$$

where ζ is the upwind sensor that is computed locally as a function of the velocity gradients and restricts the usage of upwinding scheme in dilatationally dominant regions of the domain. Using the minimum of limiter functions ϕ_L and ϕ_R reduces central blending in regions where slope limiter is active. $\alpha = 0$ corresponds to pure central formulation whereas $\alpha = 1$ recovers pure upwind.

The central blending can optionally be applied to all components of the primitive state variables, e.g. (p, u, v, w, T), or it can be applied to only the velocity components (u, v, w). We denote the former choice as CentralQ and the latter as CentralV. Unless otherwise noted, the rest of the paper utilizes the CentralQ scheme with no upwind sensor ($\zeta = 0$) or limiter ($\phi_L = 1$, $\phi_R = 1$).

B. Diffusive Flux

In order to evaluate the diffusive fluxes, primitive variable gradients at face centers are needed. The naive approach to get the face center gradients would be to simply take the average of left and right cell center gradients as:

$$\nabla \overline{Q}_f = \frac{1}{2}\left(\nabla Q_{L,c} + \nabla Q_{R,c}\right) \tag{5}$$

However, this approach is not stable and leads to the well-known even-odd decoupling issue which can be remedied via various approaches as summarized by Jalali et al. [32]. Here, we correct the face-averaged gradient in the face normal direction as:

$$\begin{aligned} \nabla \overline{Q}'_f = & \nabla \overline{Q}_f \\ & - \left(\nabla \overline{Q}_f \cdot \hat{n}\right) \hat{n} \\ & + \left(\frac{Q_{R,c} - Q_{L,c}}{d_\perp}\right) \hat{n} \end{aligned} \tag{6}$$

where $d_\perp$ is the distance between the left and right centroids in the face normal direction:

$$d_\perp = (\vec{x}_R - \vec{x}_L) \cdot \hat{n} \tag{7}$$

This treatment essentially replaces the face normal component of the face-averaged gradient $\nabla \overline{Q}_f$ with a directional derivative calculated using the two neighbor cells. The corrected face gradient $\nabla \overline{Q}'_f$ is then used to evaluate the stress tensor at the face and calculate the diffusive flux.

Subgrid scale turbulence is modeled via the Vreman model[33] with a constant coefficient of 0.08. Under-resolved boundary layers are modeled using an explicit wall function [34]. Wall function inputs are sampled at the first cell centroid off the wall.

C. Time Integration

Time integration is carried out using an explicit, 3 stage, 3$^{\text{rd}}$ order strong stability preserving Runge-Kutta scheme [35]. For a Cartesian grid, the CFL number can be defined as [36]:

$$\text{CFL} = \Delta t \left(\frac{|u| + a}{h_x} + \frac{|v| + a}{h_y} + \frac{|w| + a}{h_z}\right) \tag{8}$$

where u, v,w are the velocity components and h_x, h_y, h_z are the edge lengths in the 3 directions, while a is the local speed of sound and Δt is the time step size.

Instead of 3 distinct directions as in the Cartesian case, for a general polyhedral cell we define CFL analogously for each cell face as:

$$\begin{aligned} \text{CFL}_L &= 3\Delta t \frac{\left|\vec{V}_L \cdot \hat{r}_L\right| + a_L}{h_L} \\ \text{CFL}_R &= 3\Delta t \frac{\left|\vec{V}_R \cdot \hat{r}_R\right| + a_R}{h_R} \\ \text{CFL}_f &= \max\left(\text{CFL}_L, \text{CFL}_R\right) \end{aligned} \tag{9}$$

where $\vec{V}$ is the velocity vector, $\vec{r}$ is the vector from cell center to face center as defined in Eq. 3, and $\hat{r}$ is $\vec{r}$ normalized by its magnitude. We define the unstructured cell length scale as $h = 2\|\vec{r}\|$, i.e. twice the magnitude of the vector from cell center to face. The global CFL_{max} is then taken as the maximum of all face CFL_f values. The viscous contribution is omitted in computation of the CFL number. The global CFL_{max} value is calculated at each time step and the step size Δt is adjusted to match the user specified CFL limit.

III. Voronoi Mesh Generation

Voronoi meshes have numerous inherent properties that are ideally suited to CFD applications requiring high resolution and low dissipation on unstructured meshes while requiring minimum human effort in the mesh generation process.

A Voronoi diagram is a collection of planar faces dividing the space between points distributed in 3D space. The points are often referred to as seed points or generating locations. The faces enclosing each seed point contain the space that is closer to the seed than any other point. The faces form arbitrary polyhedral shaped cells with three key properties:

- The faces forming the cells are planar. This property is significant for cell-centered finite volume schemes which numerically treat the cell faces as flat planes with an effective normal vector, face area and centroid location. Other arbitrary polyhedral unstructured meshing approaches commonly used in CFD today do not, in general, guarantee this planarity property.
- Faces are orthogonal to the vector connecting the two generating seeds on either side of the face. This property is distinctly beneficial for the stability of the of the diffusive flux scheme as described in Section II.B.
- Faces are halfway between the seeds points on either side. This property offers multiple advantages. Face-averaging that is used in gradient calculations and diffusive flux discretization can be conducted via simple arithmetic average of cell center values on either side of the face. This results in an accurate and robust cell-center gradient method [28]. With regular seeding patterns, this property gets translated into truncation error cancellation, resulting in a non-dissipative central scheme as will be demonstrated in Section IV.A.
- Cells are guaranteed to be convex, which is among the common assumptions finite-volume solvers make, often requiring numerical treatment for non-convex cells in order to ensure stability.

All of these properties are major factors for improving the accuracy and robustness of cell-centered finite volume solvers. A caveat here is that for a randomly distributed point cloud, the resulting Voronoi mesh is not centroidal, meaning that the seed location and the resulting cell's volumetric centroid do not necessarily coincide. This in turn means that the benefits of the second and third items listed above would not be fully realized. Luckily, the point cloud can be generated in regular patterns that form centroidal Voronoi cells. This is typically done via seeding the points in a regular lattice via various arrangements. In this paper, we will focus on:

- Cartesian seeding, generating cubic cells
- Body centered cubic (BCC) seeding, generating truncated octahedron cells
- Face centered cubic (FCC) seeding, generating rhombic dodecahedron cells

The resulting cell types are illustrated in Figure 2.

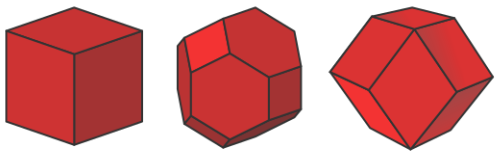

Fig. 2 Single cell view of various types: hexahedron (left), truncated octahedron (middle), rhombic dodecahedron (right)

In practical cases where there are regions of different cell sizes in the domain, the cells in the interface between the regions are not necessarily centroidal. Commonly used Lloyd's smoothing procedure [25] can be used to improve the centroidal property of the cells in this limited transition zone as well as providing a smoother gradation of cell sizes across the interface. Lloyd's smoothing procedure simply computes the centroid of the current cell shape and updates the generating seed position to coincide with the current centroid. In an iterative loop, cells approach uniformity and a centroidal shape. An illustration of the Lloyd smoothing procedure is provided in Figure 3. The initial random distibution of points yields Voronoi cells whose centroids are not coincident with the seed locations. After 20 iterations, the cells become almost perfectly centroidal with a much more even spacing.

For explicit time integration schemes, such as the one utilized here, it is important to control the minimum cell size in order to avoid excessively small time step restrictions due to the CFL constraint. Commonly used commercial unstructured grid generators typically offer little to no control over the smallest allowed cell size. In contrast, this can be tightly controlled with Voronoi meshes.

Yet another critical benefit of Voronoi meshes is that the generation algorithm can be implemented in a highly

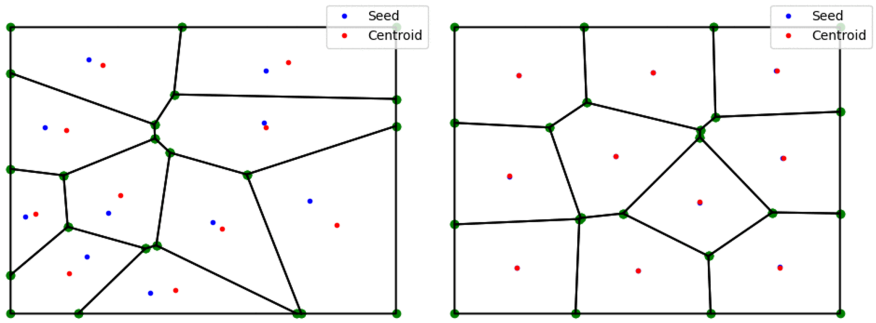

Fig. 3 Illustration of the Lloyd smoothing procedure. (left) initial, (right) after 20 iterations.

scalable manner for distributed memory parallel architectures. This enables application of Voronoi meshes for highly resolved large eddy simulations requiring on the order of hundreds of millions to billions of computational cells.

Throughout this work, we utilize fully isotropic mesh generation. Although anisotropy can be implemented with Voronoi meshing approaches, isotropy is preferable for LES.

The final step in the Voronoi mesh generation is to clip the cells that are intersected by the geometry, provided to the mesher in the form of a surface triangulation. In order to avoid irregular clipped near-body cells, we align the seeds along iso-contours of wall distance for a user specified number of seed layers. Please note that for the clipped cells adjoining the geometry, many of the properties listed above (e.g centroidality, face planarity and orthogonality) necessarily break down. However, for wall-modeled LES simulations, diffusive fluxes at the body faces are directly imposed by the wall function and hence they are less susceptible to the imperfections in cell geometry.

Analyses in the following sections utilize Voronoi meshes created using LAVA Voronoi mesher developed in-house at NASA Ames Research Center.

IV. Results

A. Isentropic Vortex Propagation

The isentropic vortex propagation test case consists of an inviscid vortex being advected by a constant velocity mean flow, $\overrightarrow{U} = [u_0, v_0]$, in a given direction. The setup is described by Hu *et al.* [37]. Here, however, the problem is slightly modified to use a vortex tube traveling through a 3D periodic domain with both uniform meshes and coarse-fine interfaces. This change allows studying the effects of different three-dimensional Voronoi seeding strategies and the corresponding cell-types in a canonical test case.

1. Uniform meshes

The computational domain used to analyze the isentropic vortex propagation through uniform grids extends from $[-2, -2, -2h]$ to $[2, 2, 2h]$, where h is the cell spacing. The computational setup is illustrated in Figure 4. Various mesh types and resolutions considered in the current study are listed in Table 1. Please note that for the same domain and the same spacing size, Voronoi BCC meshes have 2 times as many cells and 4.67 times as many faces as the Cartesian mesh. For the Voronoi FCC type mesh, these factors increase further to 4 times as many cells, and 8 times as many faces. Considering that the computational cost for our scheme closely scale with the number of faces (and hence the number of flux evaluations), Voronoi BCC, and to an even greater extent, Voronoi FCC meshes are significantly more expensive to compute compared to a Cartesian mesh of same spacing.

Unless otherwise specified, the CentralQ convective flux formulation is used with no limiter or upwind sensor (see Section II.A). In order to isolate the effects of spatial discretization, time step size is selected conservatively small at $\Delta t = 1.25 \times 10^{-4} T$ where $T = L/u_0$ is the period of one vortex pass-through the domain.

The vortex travels in the x direction with a background flow velocity of $\overrightarrow{U} = [0.5, 0.0]$. Figure 5 shows the pressure contours for initial conditions (shown in blue) and after 5 vortex pass-through periods (shown in red) for the different mesh types considered. The vortex drift is immediately noticeable, especially on coarser resolutions, while the vortex strength and shape remain intact. This is an expected result since the central second order scheme has a kinetic energy

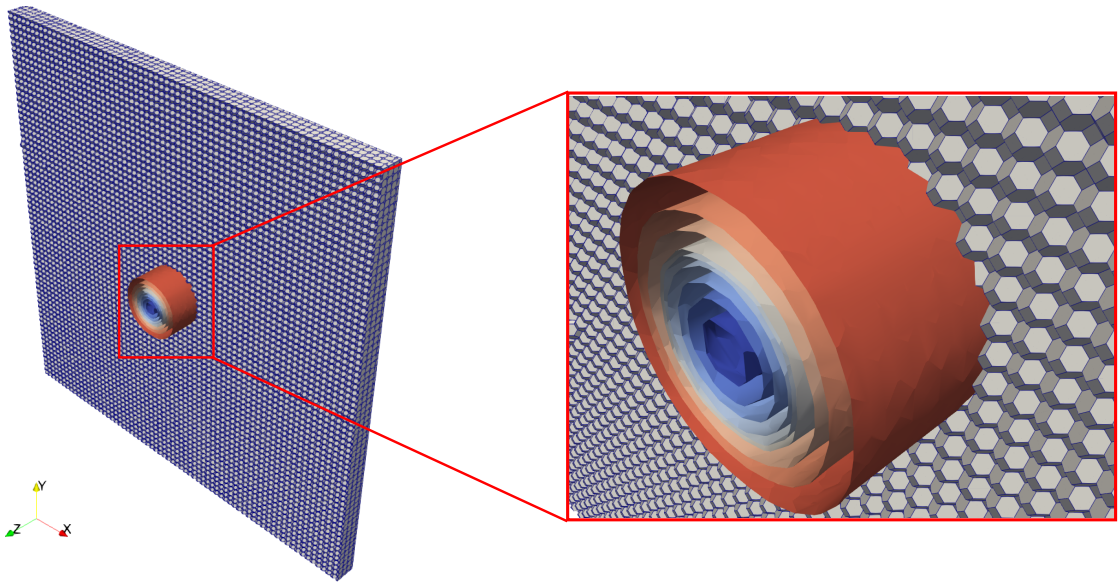

Fig. 4 Initial vortex pressure iso-contours in the domain cutout shown for the Voronoi BCC mesh with $N = 64$ cells in the x and y directions, i.e. $h = 1/16$.

Table 1 Meshes used for the isentropic vortex propagation test.

Name	Cell Type	Spacing (h)	# Cells (N_c)	# Faces (N_f)
Cartesian	Hexahedron	1/16	16,384	49,152
		1/32	65,536	196,608
		1/64	262,144	786,432
Voronoi BCC	Truncated octahedron	1/16	32,768	229,376
		1/32	131,072	917,504
		1/64	524,288	3,670,016
Voronoi FCC	Rhombic dodecahedron	1/16	65,536	393,216
		1/32	262,144	1,572,864
		1/64	1,048,576	6,291,456

preserving property which leaves dispersion as the dominant source of error. When different mesh types with the same spacing (h) are considered, it can be observed that the Cartesian mesh results exhibit the largest drift followed by Voronoi BCC and Voronoi FCC. Although the same spacing is used to generate these grids, the different sphere packing configurations allow for denser tessellations of the computational domain with BCC and FCC (when compared against the Cartesian seeding) at the expense of an increased number of cells and faces (as listed in Table 1). The overall effect is a smaller discretization error at the same spacing (h) but with an increased computational cost. Moreover, it can be observed in Figure 5, that all the simulated results qualitatively approach the analytical solution as the grids are refined.

In all simulations performed with the CentralQ scheme, the vortex strength has been preserved through the 5 periods tested. This is better observed in Figure 6 (left) which shows the time history of the integrated kinetic energy, where the initial kinetic energy remains constant, regardless of the mesh type. In contrast, the upwind scheme result shown for the Cartesian mesh with $h = 1/16$ shows decay of the kinetic energy as expected. Figure 6 (right) contains results for the L_∞ norm of the pressure error with respect to analytical solution. For cases which relied upon the CentralQ scheme and its kinetic energy preservation characteristic, the error can be directly attributed to either distortion or drift of the vortex. For such cases, apart from an initial adjustment of the numerical solution on the discretized meshes, a constant rate of error accumulation throughout the time history is observed and the error levels are consistent with the drift magnitude observed in Figure 5. For the coarse Cartesian result, a flattening of the error accumulation can be observed

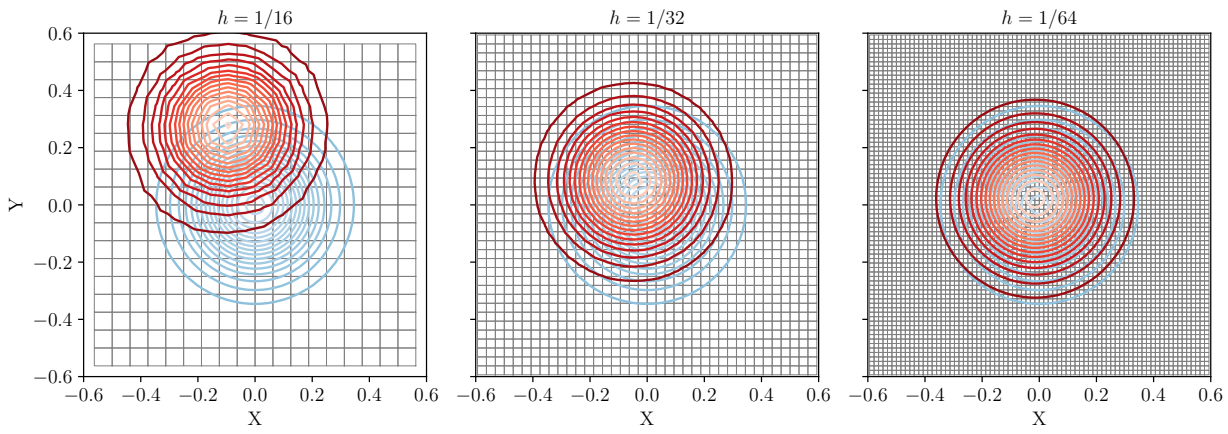

(a) Cartesian

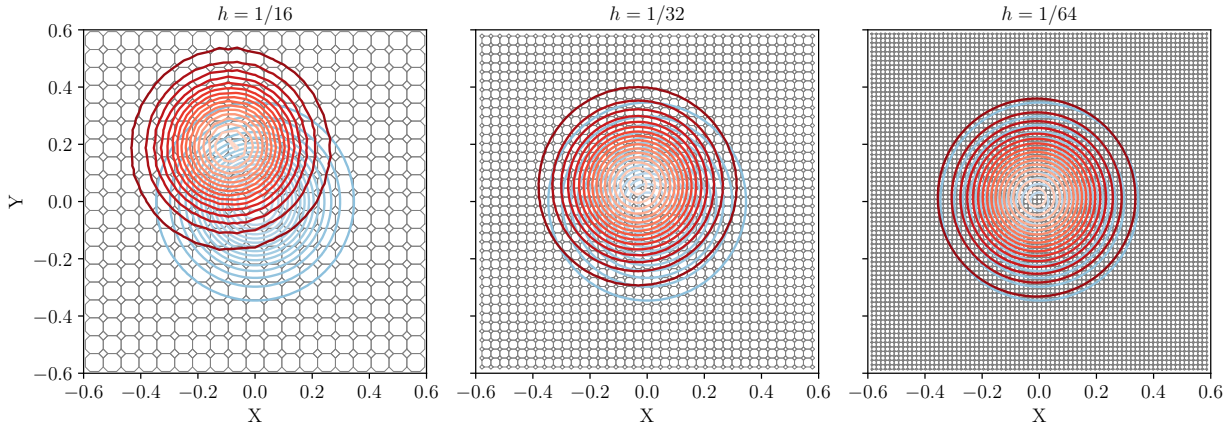

(b) BCC Seeding

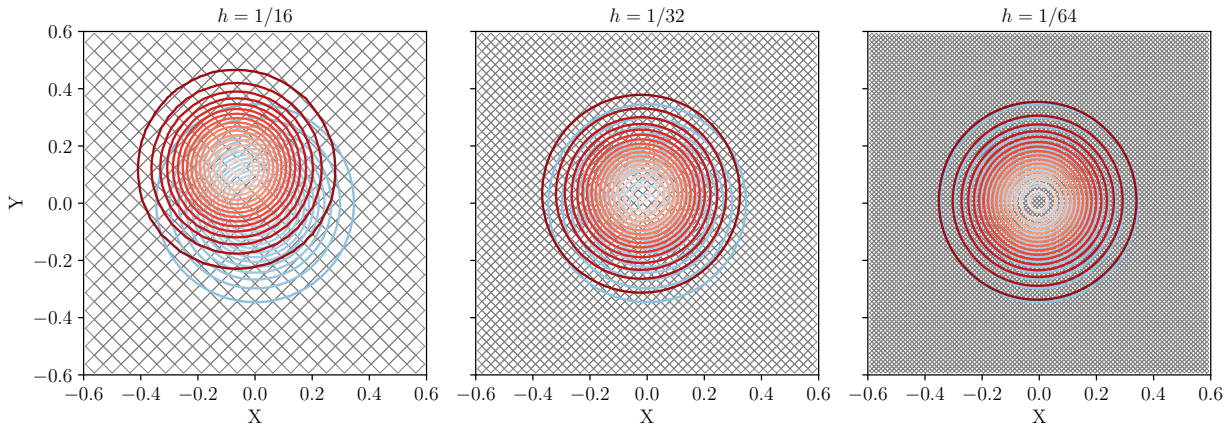

(c) FCC Seeding

Fig. 5 Pressure contours for initial conditions (blue) and after 5 vortex pass-through periods (red). Focus is given to the region near the center of the domain with $X, Y \in [-0.6, 0.6]$.

for pass-through periods greater than 3. This is due to the large drift of the vortex, resulting in little to no overlap with the analytical solution and hence saturating the error. Between the CentralQ solutions with the same mesh spacing, the

Cartesian results exhibit the largest error, followed by BCC and FCC meshes. The error for the upwind scheme, both dissipative and dispersive in nature this time, grows much more rapidly and reaches the saturation level sooner.

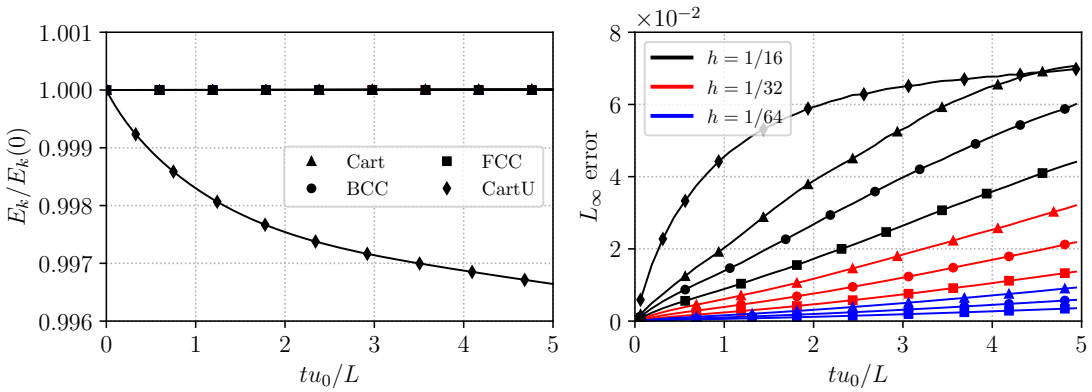

Fig. 6 Non-dimensional integrated kinetic energy (left) and L_∞ norm of the pressure error (right) history over 5 vortex pass-through periods. All simulations were run with the CentralQ scheme except 'CartU', which was computed using the upwind method.

2. Coarse-fine interface meshes

The computational domain used to analyze the isentropic vortex propagation through a refinement interface differs from the ones used in the case of uniform meshes. A periodic cubic domain with an edge length of 4 centered around zero was chosen. The domain included a refinement region contained in a smaller cube with unitary edge length. This change allowed us to retain a perfect periodic overlap in all directions, free from the influence of coarse/fine interface smoothing. A BCC seeding strategy is used with spacings of $h = 1/16$ in the coarse region and $h = 1/32$ in the fine region.

The Lloyd procedure (see Section III) with varying number of iterations is used to smooth the coarse/fine interface, spreading the cell size transition over multiple layers of cells as opposed to an abrupt change. The initial mesh (0 Lloyd iterations), as well as the mesh after 500 Lloyd iterations are shown in Figure 7. Also shown is the normalized cell volume distribution through the refinement interface region along the x axis for various numbers of Lloyd iterations. It can be observed that the transition from fine to coarse becomes increasingly more gradual as the number of iterations increase.

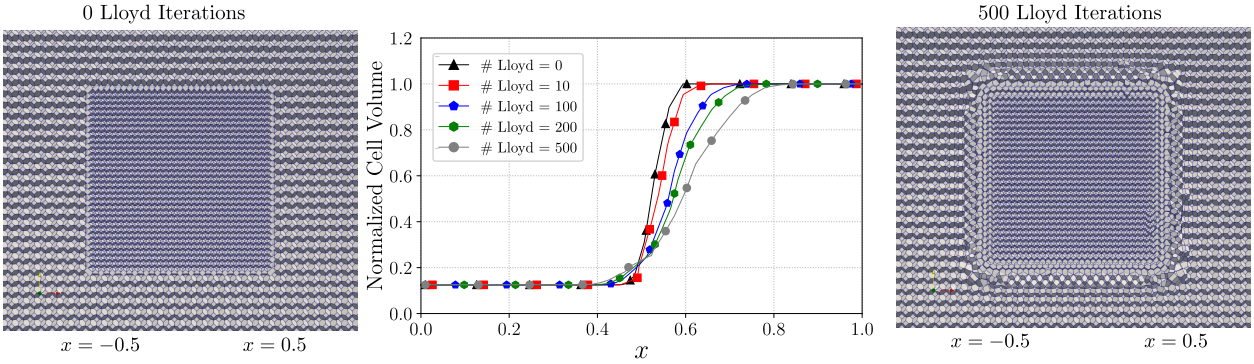

Fig. 7 Effect of Lloyd smoothing on the coarse ($h = 1/16$) - fine ($h = 1/32$) interfaces.

This test case being inviscid and the CentralQ scheme being kinetic energy preserving, any discretization error generated in the advection through the coarse fine interface is expected to accumulate, rendering the simulation noisy and unstable if no further treatment is adopted. Therefore the Vreman Sub-Grid Scale (SGS) model is utilized here to help attenuate the high wave number errors.

The integrated kinetic energy history as well as the L_1 and L_∞ norms of the pressure error are shown in Figure 8. When SGS is off, we observe that the kinetic energy is preserved even with existence of the coarse/fine interface. However, the pressure error rapidly climbs due to deformation and drift of the vortex. When SGS is activated, the kinetic energy decay is apparent as expected, but the pressure error rise is more controlled and the vortex retains a coherent shape. Please note that in practical LES simulations, molecular viscosity as well as the upwind sensor also act to reduce spurious oscillations, as will be shown in Section IV.C.

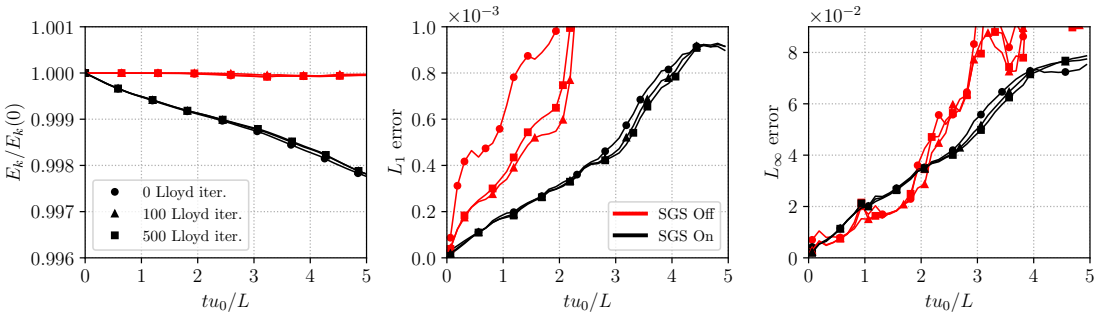

Fig. 8 Kinetic energy (left) as well as L_1 (center) and L_∞ (right) pressure error norms as a function of time for the isentropic vortex advecting through coarse fine interfaces with different number of Lloyd smoothing iterations. Results are shown for a mesh composed of two BCC regions with spacings of $h = 1/16$ and $h = 1/32$.

Figure 8 also reveals that with increased number of smoothing iterations, the error accumulation rate decreases consistently (until late stage saturation and flattening of the error curve as discussed above). However this effect is marginally small. Same observation can be made via Figure 9 where the vortex structures are similar between the non-smoothed and smoothed interfaces of different number of iterations. The non-smoothed case, however, shows a greater tendency to accrue spurious content at the coarse/fine interface as well as a slightly faster decay of the vortex. Another observation is that as the drift promoted by dispersion errors accumulates, the vortex core moves in the positive y direction and approaches the upper coarse-fine interface region. Once part of the core starts propagating along the transitional region, the energy dissipation rate (as seen in Figure 8) slightly accelerates.

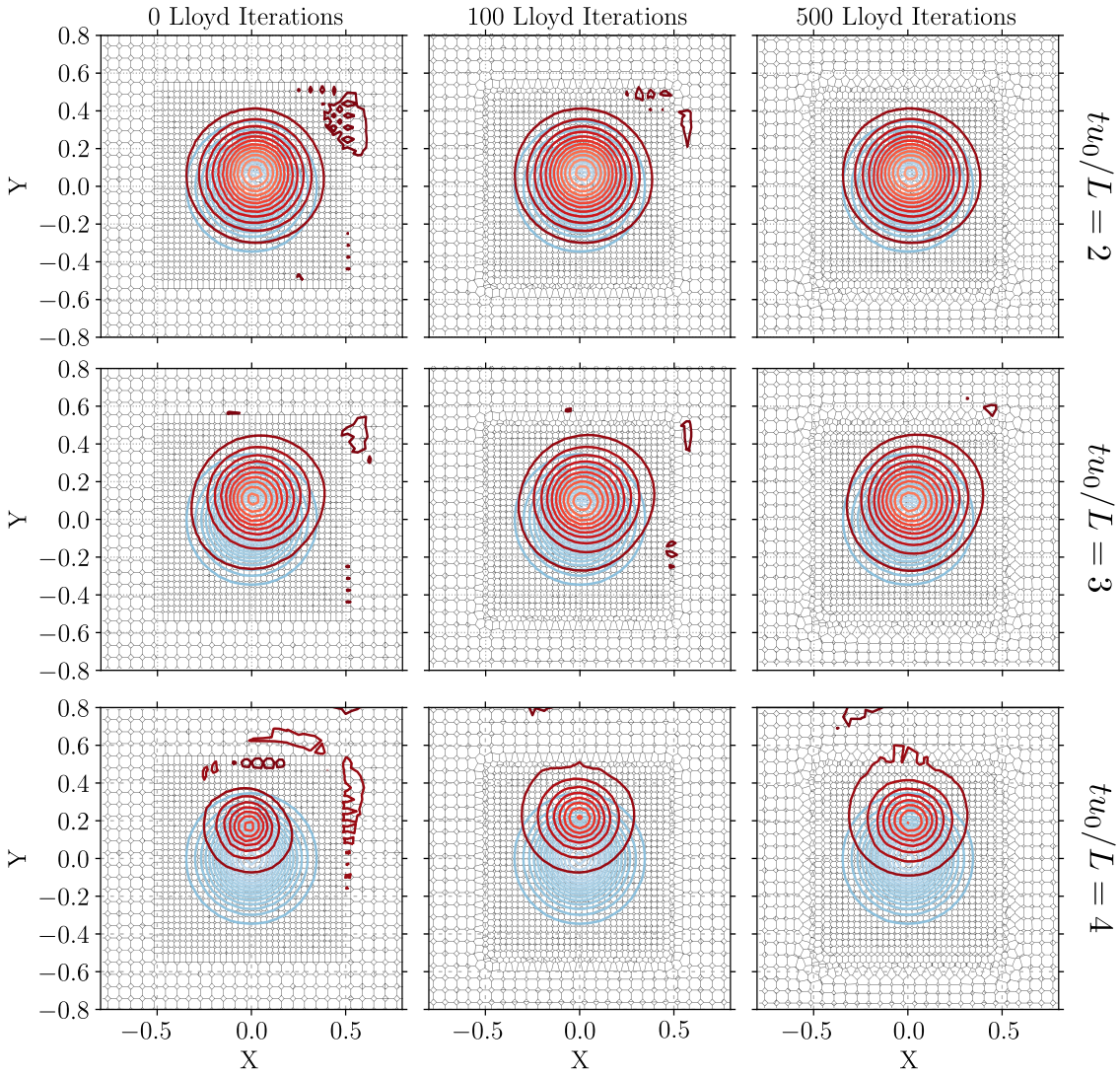

Fig. 9 Pressure contours for initial conditions (blue) and after 2, 3 and 4 vortex pass-through periods (red) for a vortex propagating through a coarse ($h = 1/16$) - fine ($h = 1/32$) interface.

B. Homogeneous Isotropic Turbulence

The purpose of studying the forced Homogeneous Isotropic Turbulence (HIT) problem at an asymptotically high Reynolds number ($\mathrm{Re}_\lambda \to \infty$) is to demonstrate: a) Non-dissipative character of the inviscid flux discretization, and b) Robustness and dissipation rate accuracy provided by the diffusive flux discretization of the SGS model.

A triply periodic domain with extents from $[0, 0, 0]$ to $[1, 1, 1]$ is used. While a statistically identical stationary state can be reached with any non-zero initial condition, in the present case the flow is initialized with the Taylor-Green vortex as described in Carton et al. [38] so that the initial flow field is divergence free (single-mode) - and hence avoids occurrence of spurious acoustics due to initial transience. At the asymptotic state the turbulent Mach number is $M_t < 0.2$ and hence no-shock capturing is needed due to absence of shocklets. A momentum forcing source term is used as[39]:

$$S_i = \rho u_i C_f \frac{E_{\text{target}}}{E(t)} \quad \text{for} \quad i = 1, 2, 3 \tag{10}$$

where ρ is the density, u_i is the velocity component, $C_f = 0.01$ is the forcing constant, $E_{\text{target}} = 5 \times 10^{-5}$ is the target non-dimensional integrated kinetic energy, and $E(t)$ is the instant non-dimensional integrated kinetic energy. The forcing term allows energy production and dissipation to settle into an equilibrium after the decay of the initial energy.

The CentralQ convective scheme with no upwind sensor or limiter was used (see Section II). The Vreman SGS constant used was 0.08. A maximum CFL number of 1.5 was used for all cases.

Three different uniform Voronoi meshes were investigated; Cartesian, BCC and FCC seeded. Each was run at two resolution levels with spacings of: $h = 1/32$, and $h = 1/64$. The Cartesian mesh was also run with $h = 1/128$ to serve as reference; the dissipation rate set by the source term is identical in each case simulated.

The results for energy spectra are shown in Figure 10 for all mesh types. For each mesh type, energy decay rate in the inertial range follows the correct slope due to Kolmogorov's hypothesis, indicated with the solid black, $k^{-5/3}$ line. For each case, the onset of rapid energy dissipation at the subgrid scale is captured at correct Nyquist wave numbers as shown with vertical black lines. Note that the energy pile up, or loss in the case of FCC, near the Nyquist wave number is attributed to the procedure of interpolating the solution on to a uniform mesh in order to perform fast Fourier transform.

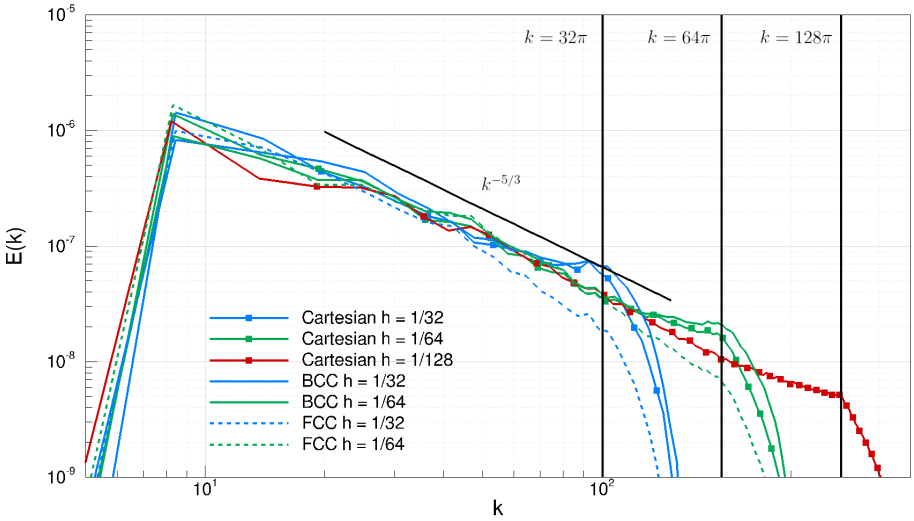

Fig. 10 Turbulent energy spectra for decay of homogeneous isotropic turbulence for Cartesian meshes (upper) and Voronoi meshes (lower).

C. 30P30N Multi-Element Airfoil

McDonnell Douglas 30P30N multi-element airfoil is an experimental setup [40] that has widely been adopted as a CFD benchmark case for high-lift wing configurations [41–44]. The setup is a constant-profile, unswept wing with a leading edge slat and a single-element flap. With the available measurements of aerodynamic loads data as well as surface pressures at a realistic high-lift flow regime of Ma = 0.2 and Re = 9×10^6, it is a great test bed for the WMLES numerical schemes and the unstructured meshing methods presented here.

An overview of our mesh sizing approach for 30P30N is shown in Figure 11. Refinement regions are generally setup to cover bands of wall-distance. The finest region is located next to all the wing surfaces except the main element lower surface where flow is known to stay attached. The finest region covers about $0.15c$ distance from the walls (where c is the stowed airfoil chord length) and the cells in this zone are sized to have a spacing of $0.0005c$. The spacing doubles in the next region, and for each subsequent region with growing wall distance, the spacing increases by a factor of 1.5. A box shaped region was added to avoid coarsening too soon in the wake. The domain boundary extends to $100c$ in both directions. The mesh is created in $2D$ and extruded along the span, using a spacing of $0.001c$, for 100 layers covering a span length of $10\%c$. Periodic boundary condition is applied at the span end planes.

The computational meshes were generated with our in-house LAVA Voronoi meshing tool, using a clipped Voronoi tessellation with two different seeding types: Cartesian and hexagonal. A close-up view of the resulting meshes is shown near the slat trailing edge in Figure 12. The seeds near walls have been aligned into four wall layers. The cells near refinement region interfaces have been smoothed using the Lloyd iteration method, which naturally changes the shape and size of these transition cells in order to converge towards a centroidal cell shape (where the generating seed and cell centroid locations coincide). For Cartesian seeded meshes, cells in the smoothing zones (which include the wall

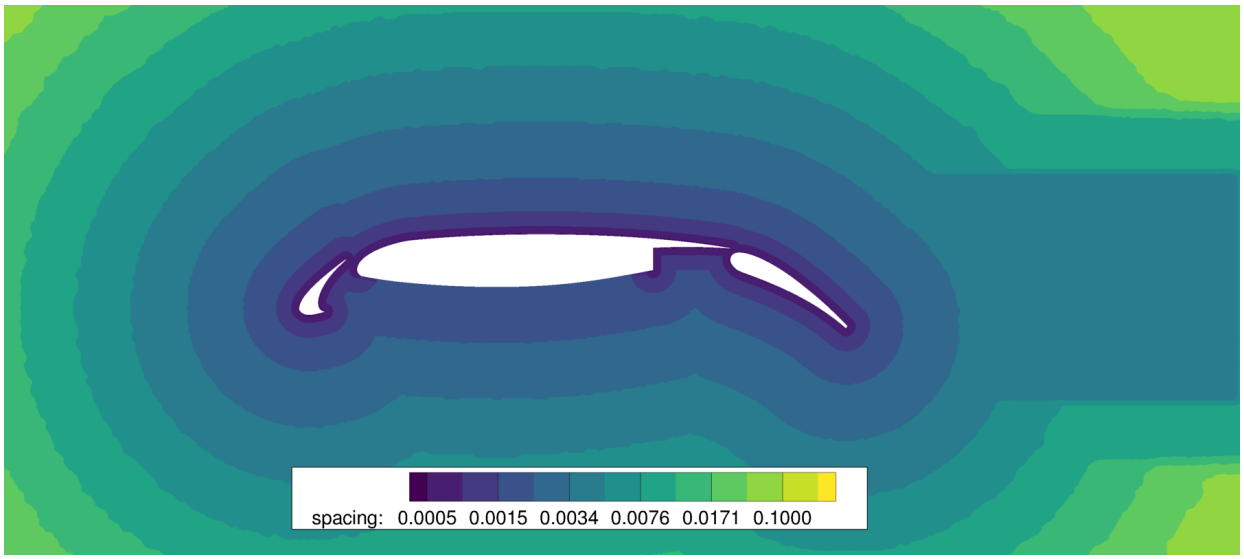

Fig. 11 Computational mesh sizing overview for 30P30N.

layers) naturally tend towards hexagonal and transitional shapes during smoothing. This introduces a cell type transition in region interfaces. On the other hand, the hexagonal seeded mesh exhibits much more consistent cell shapes.

All of the meshes tested are made up of isotropic cells with the exception of spanwise spacing. The spanwise extrusion of the 2D mesh was done using a spacing of $0.001c$ for all meshes as listed in Table 2. As a result, the extrusion introduces anisotropy away from the walls where the cells get larger on the 2D plane. At the wall, the coarse Cartesian seeded mesh is isotropic in spanwise direction whereas the fine Cartesian and Hexagonal seeded meshes have spanwise aspect ratio of 2.

A summary of near wall spacings and the total number of cells and faces for each mesh is listed in Table 2. The coarse version of the Cartesian seeded grid is generated by simply turning-off the finest near-wall sizing region while keeping the rest of the mesh identical.

Table 2 Near-wall mesh spacings, and number of cells and faces for 30P30N.

	Spacing (chord normalized)					# Cells	# Faces
Mesh	Slat	Main Upper	Main Lower	Flap	Spanwise	(million)	(million)
Cartesian Voronoi - Coarse	1e−3	1e−3	2e−3	1e−3	1e−3	31.8	101.3
Cartesian Voronoi	5e−4	5e−4	2e−3	5e−4	1e−3	41.7	133.8
Hexagonal Prism Voronoi	5e−4	5e−4	2e−3	5e−4	1e−3	50.9	198.3

Simulations were run at angles of attack of $\alpha = 8.10°, 16.21°, 21.34°$ and $23.28°$ corresponding to the cases listed by Klausmeyer and Lin [43] for Ma = 0.2 and Re = 1×10^9. For all the runs, the CentralV scheme was used along with the upwind sensor as described in Section II. Vreman subgrid scale model [33] was utilized with a model constant of 0.08.

Simulations were carried out until statistical convergence of the lift coefficient was attained. The hexagonal mesh cases were impulsively started from free-stream conditions and were simulated to about 100 convective time units (CTU) calculated based on the free-stream velocity and stowed chord length. The coarse Cartesian mesh cases were also impulsively started but the convergence required a significantly longer time integration interval between 170 to 240 CTUs. The Cartesian fine mesh cases were started with interpolated results from corresponding Cartesian coarse mesh cases and required an additional time integration interval of about 80 CTUs.

Instantaneous velocity magnitude contours of solutions on the Hexagonal Voronoi mesh are shown in Figure 13 for each angle of attack. For all angles of attack, slat wake is prominent, with increased intensity and larger scale turbulent structures at higher angle of attacks. At $\alpha = 21.34°$ and $23.28°$, the slat and flap wakes merge.

At the lower two angles of attack, the slat top surface remains largely attached and laminar, whereas the higher angles of attack exhibit development of laminar separation bubbles and transition to turbulence. This can be better

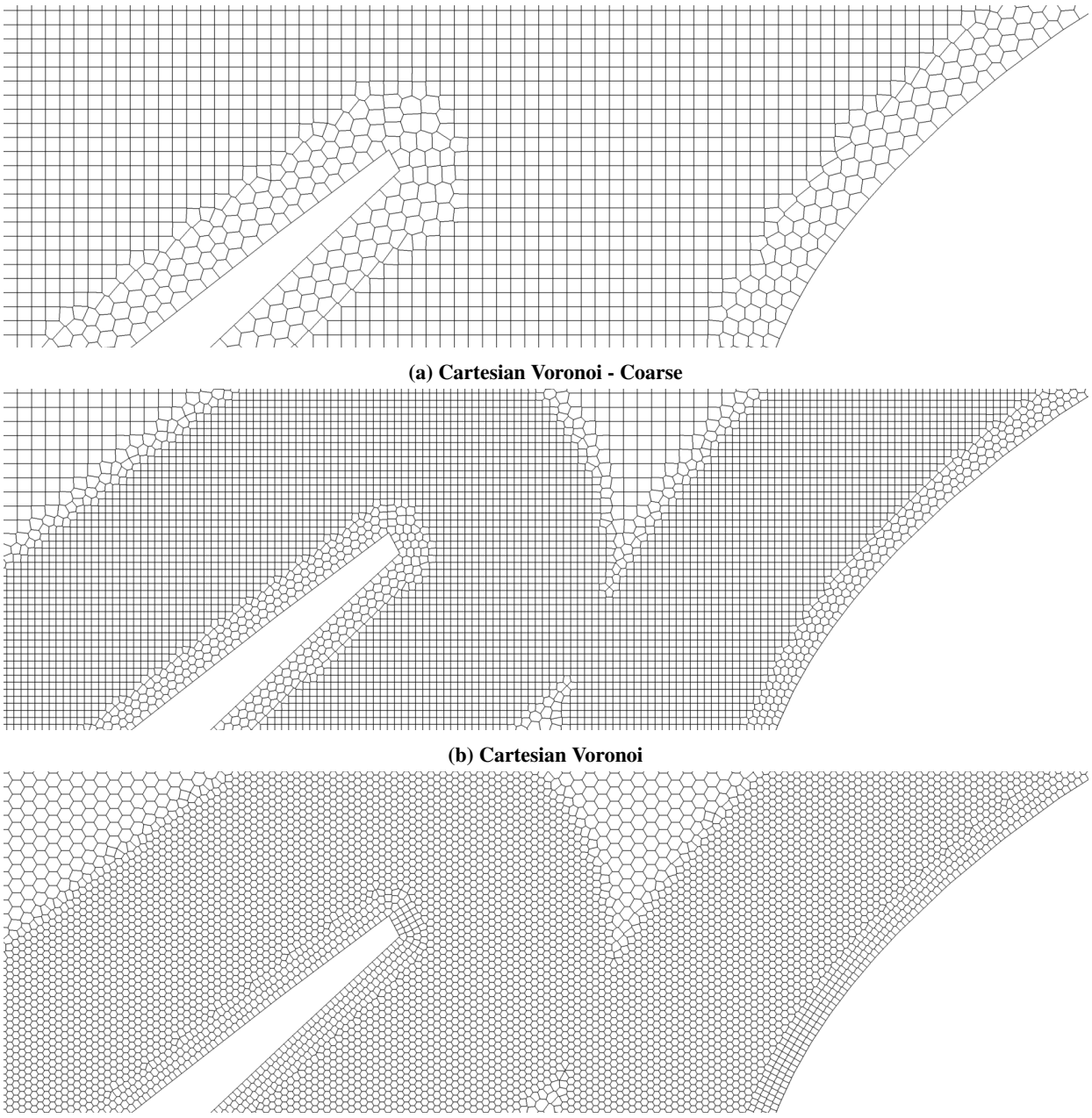

(a) Cartesian Voronoi - Coarse

(b) Cartesian Voronoi

(c) Hexagonal Prism Voronoi

Fig. 12 Computational mesh around slat gap for 30P30N.

observed in the close-up view of the solution over the slat and the main elements as shown in Figure 14 for each mesh. We immediately notice that at high angles of attack, the flow over the slat upper surface is mesh sensitive. The coarse mesh tends towards predicting a laminar separation whereas the finer meshes tend towards a break down and transition of this structure. This suggests that we could benefit from further mesh refinement in this zone, a conclusion that will also be apparent in the following results. A similar observation can be made for the main element upper surface where the finer meshes exhibit earlier transition.

Figure 15 shows the close-up views of the instantaneous flow field over the flap. Here, we don't immediately observe mesh sensitivity in terms of bulk features of the flow. However the fine mesh results, particularly the hexagonal Voronoi mesh, exhibit better definition of the turbulent structures near the top surface of the flap.

Figure 16 shows pressure coefficient, C_p, distributions in comparison to the experimental measurements (digitized from Klausmeyer and Lin [43]) for each angle of attack simulated. The simulation pressure distributions are extracted at the mid-span from the time-averaged solution. Time averaging was carried out over 50 CTU's (Convective Time Units) starting from the point of statistical convergence of the integrated lift. A small magnitude but persistent oscillatory behavior in C_p around highly curved surfaces were noticed after time averaging was performed. Upon investigation, it was found that the resolution of the 30P30N geometry definition we utilized was coarser than our eventual mesh, leading to paneling. In retrospect, the geometry should have been splined before meshing to avoid this issue.

Overall, agreement with the experimental pressure coefficient measurements is excellent, with few exceptions. On the slat upper surface, simulations qualitatively differ from the experiments, particularly at higher angles of attack. This is not surprising because of the transitional nature of the flow over the slat. As also observed in the instantaneous velocity magnitude contours, simulations stay laminar over the suction side of the slat at lower angle of attacks. At higher angles, separation bubbles form and break down, eventually developing into turbulence. Increased grid resolution seems to yield an earlier onset of transition. In this context, we may also observe that the hexagonal mesh exhibits an effectively higher resolution compared to the Cartesian mesh even though they share the same spacing. This is consistent with the findings we discussed in Section IV.A. We note that the transitional flow over the slat, and the observed grid sensitivity, is a characteristic that is largely due to the 2D nature of the unswept wing geometry. For more realistic, swept wing configurations, the transition over the slat is further aided by the spanwise flow.

Interestingly, the coarse Cartesian mesh results over the slat seem to agree better with the experimental pressure coefficients up until the highest angle of attack. This can be explained by the fact that the boundary layer is largely missed by the wall model due to insufficient resolution of the coarse mesh, therefore not imposing enough momentum retardation to cause separation.

Over the main element, the pressure coefficient predictions are in excellent agreement with the experiments, with the coarse mesh slightly under-predicting the suction peak at high angles of attack. For all angles, the hexagonal mesh displays consistently better agreement with the experiments, although the differences between the simulations are small.

Predictions over the flap are in line with the experiment at low angles of attack. At the high angles, however, the suction peak is slightly under-predicted but with apparent convergence to the experiment with grid refinement.

Figure 17 shows the lift coefficient, C_L, values in comparison to experiments [40] and the similar WMLES study conducted by Wang et al [44]. The simulation time history of C_L for one of the cases is also shown in the figure along with the averaging period. The hexagonal mesh result has excellent agreement with the experiment with the exception of the lowest angle of attack where all simulations predicted slightly higher lift. The Cartesian mesh cases, both coarse and fine, under-predicted the lift at high angles of attack, but displayed correct convergence trend with mesh refinement.

Figure 18 and Table 3 demonstrate the effect of the upwind sensor used in the convective scheme (as described in Section II.A). These tests are shown for hexagonal mesh near $C_{\mathrm{L,max}}$ at $\alpha = 21.34°$. For the fully upwind scheme ($\zeta = 1$), flow field is largely diffused, with the slat wake remaining laminar, and the boundary layer over the upper surface of the main element only transitioning to turbulence past mid-chord location. The corresponding C_L is significantly under-predicted; a trend consistent with coarse mesh results seen in Figure 17. Due to the dissipative nature of this approach, it would take a significantly finer grid resolution to attain accurate predictions. The pure CentralV scheme ($\zeta = 0$) solution is completely contaminated with spurious noise. Although the run remains stable, the C_L is significantly over-predicted. In contrast, the CentralV scheme with the upwind sensor based blending avoids the spurious oscillations and provides accurate results. Although not strictly kinetic energy preserving, the CentralV scheme was chosen in lieu of CentralQ for the simulations in this section because, in our experience, it provides improved robustness in the presence of supersonic regions (which exist for this case at high angles of attack). We did perform a verification of this choice by restarting a CentralV run with CentralQ for $\alpha = 21.34$. No noticeable difference, qualitative or quantitative, was observed for nearly 10 CTU's, although ultimately CentralQ simulation was not stable.

Table 3 Lift coefficients for different convective scheme approaches, computed on the hexagonal prism mesh at $\alpha = 21.34$.

Scheme	C_L	Error w.r.t to Experiment
Experiment [40]	4.35	—
Pure upwind	4.05	6.8%
Pure CentralV (upwind sensor off)	4.58	5.4%
CentralV with upwind sensor	4.34	0.2%

A summary of computational costs is provided in Table 4. Please note that the metrics presented in the table exclude the periodic boundary condition which adds further 20% to the cost. Periodicity implementation in our solver has not yet been optimized because it is not critical for practical applications of high lift configurations. Instead, symmetry boundary condition was used for the timings reported here. Considering that the hexagonal mesh cases took around 100 Convective Time Units (CTU's) to complete, they can be completed in 4 days with these resources. When overall turn-around time is critical, we have seen reasonably efficient scalability up to 50 CTU's per day. Runs on the Cartesian mesh of equivalent spacing were 1.56 times faster per CTU, closely reflecting the ratio of number of faces. Although the hexagonal mesh runs were more expensive, they had an effectively higher resolution evidenced by the better agreement with the experiment.

Table 4 Computational cost summary.

Mesh	# Cells (million)	# Faces (million)	Node Type	CPU cores	Time step (s)	Wall time per step (s)	Wall time per CTU (hr)
Hexagonal	50.9	198	Intel Skylake	1200	3.85×10^{-7}	0.0925	0.961
Cartesian	41.7	134	Intel Skylake	1200	4.18×10^{-7}	0.0644	0.616

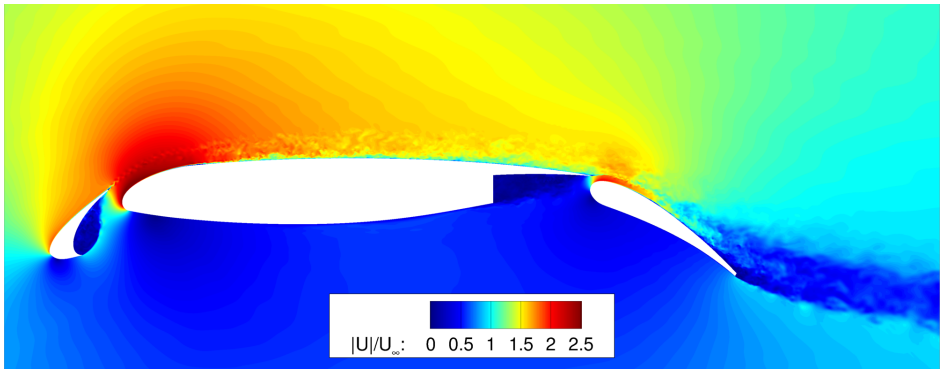

(a) $\alpha = 8.10°$

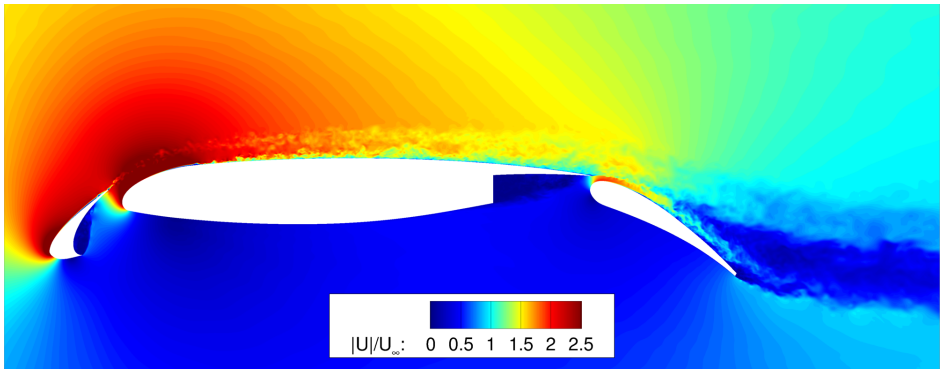

(b) $\alpha = 16.21°$

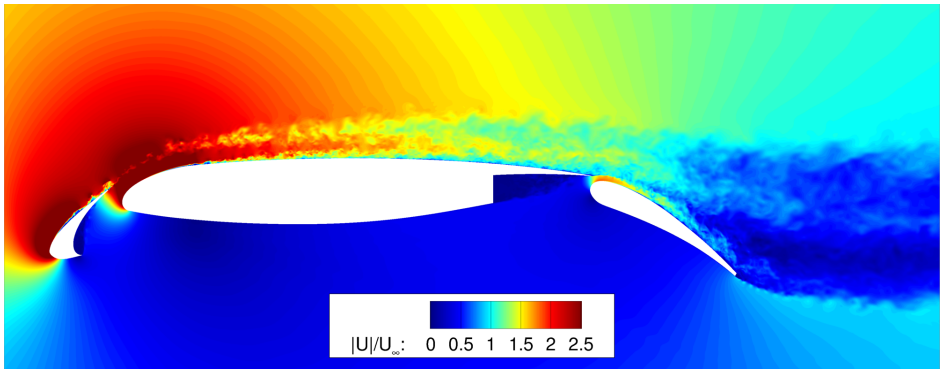

(c) $\alpha = 21.34°$

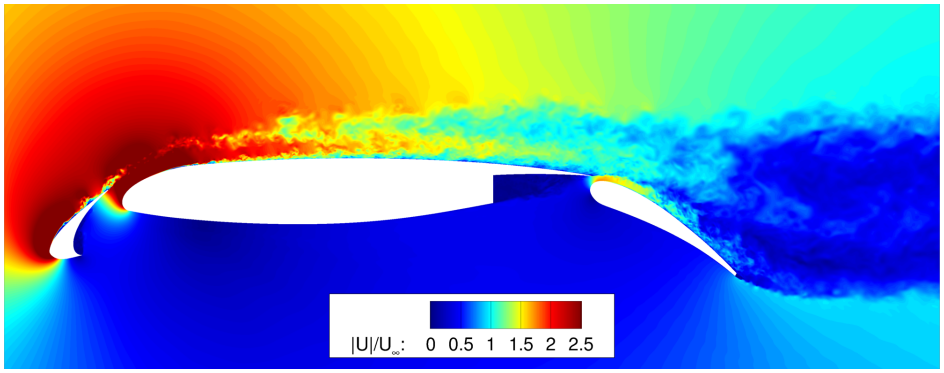

(d) $\alpha = 23.28°$

Fig. 13 Instantaneous normalized velocity magnitude contours on the hexagonal prism mesh.

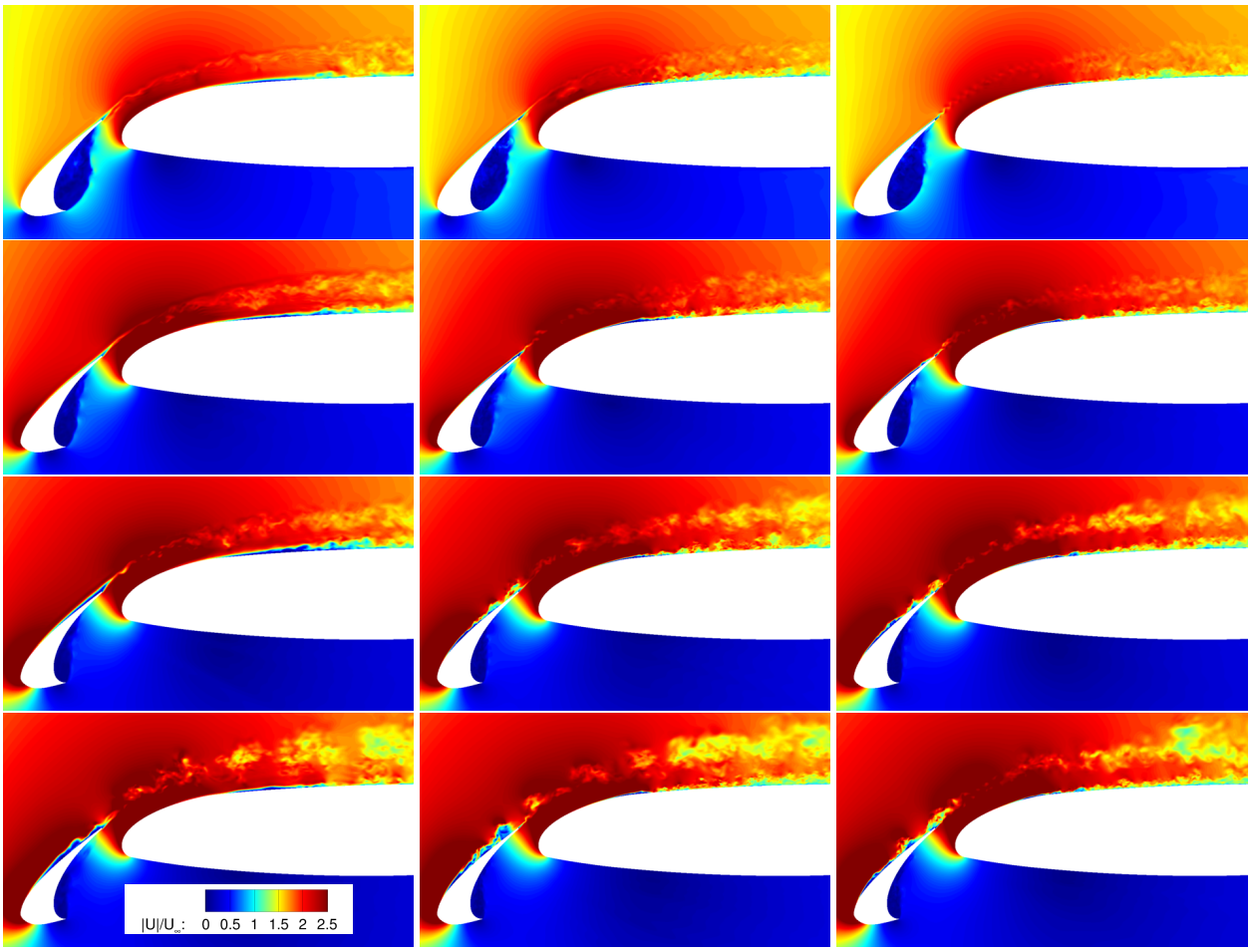

(a) Cartesian Voronoi - Coarse **(b) Cartesian Voronoi** **(c) Hexagonal Voronoi**

Fig. 14 Instantaneous normalized velocity magnitude contours, $\alpha = [8.10°, 16.21°, 21.34°, 23.28°]$ (top to bottom).

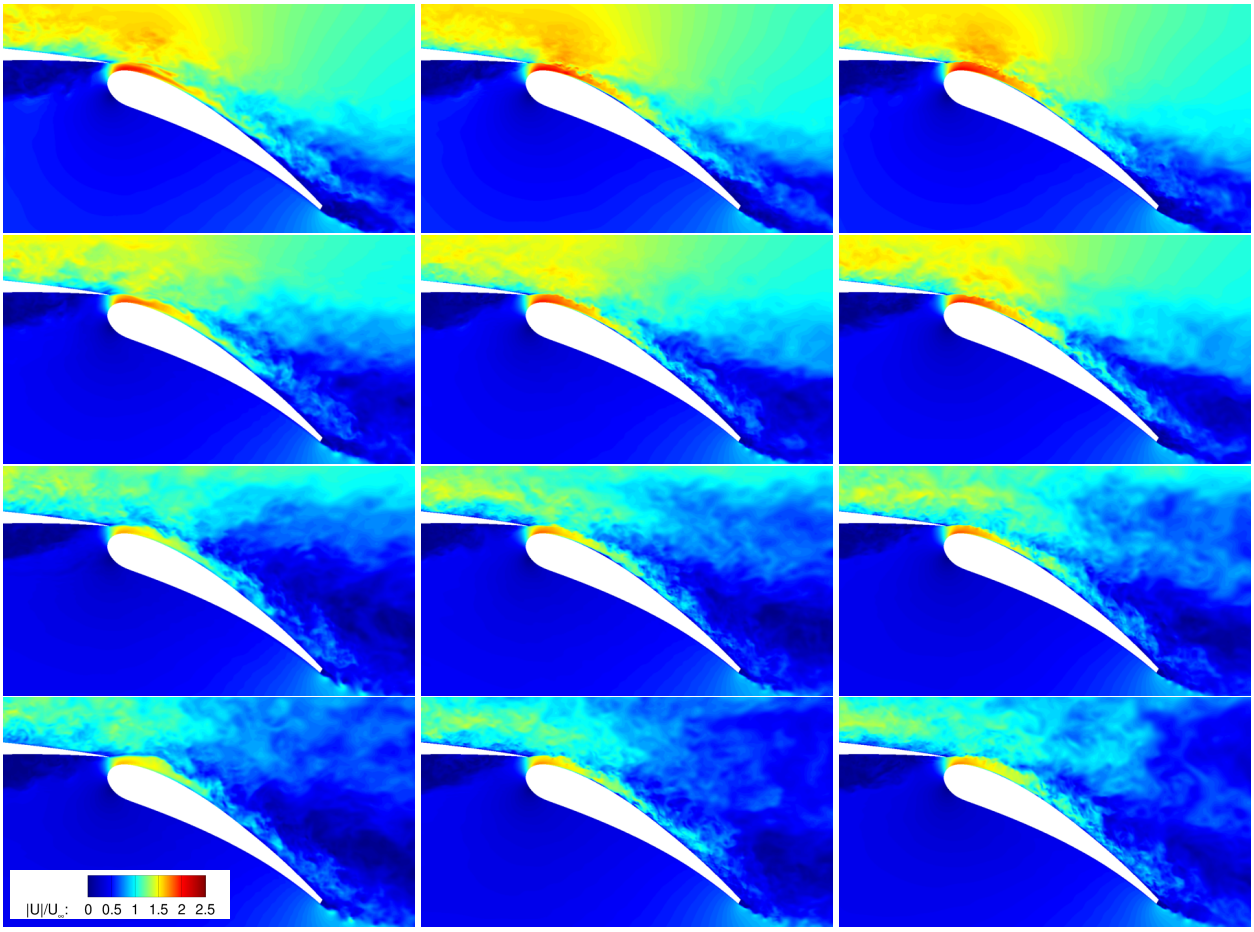

(a) Cartesian Voronoi - Coarse **(b) Cartesian Voronoi** **(c) Hexagonal Voronoi**

Fig. 15 Instantaneous normalized velocity magnitude contours, $\alpha = [8.10°, 16.21°, 21.34°, 23.28°]$ (top to bottom).

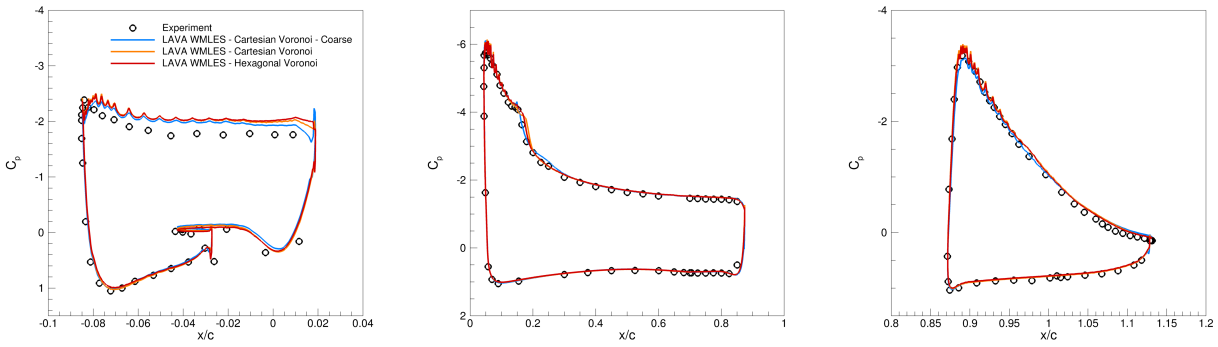

(a) $\alpha = 8.10°$

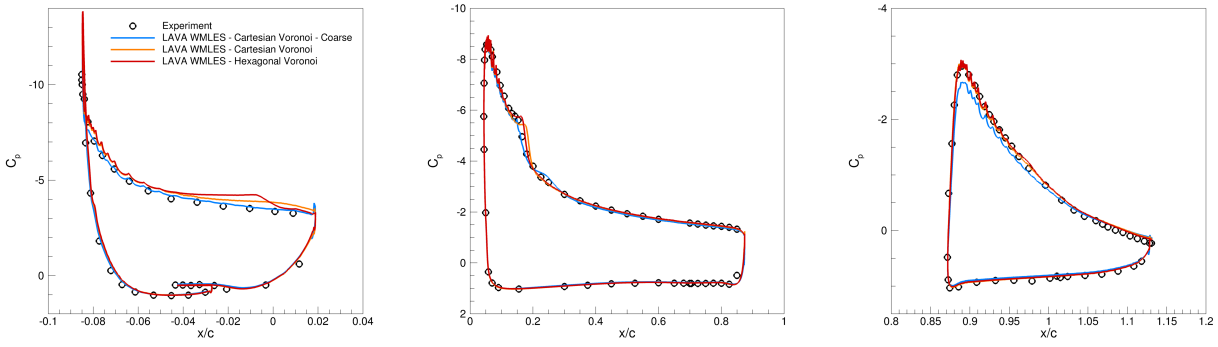

(b) $\alpha = 16.21°$

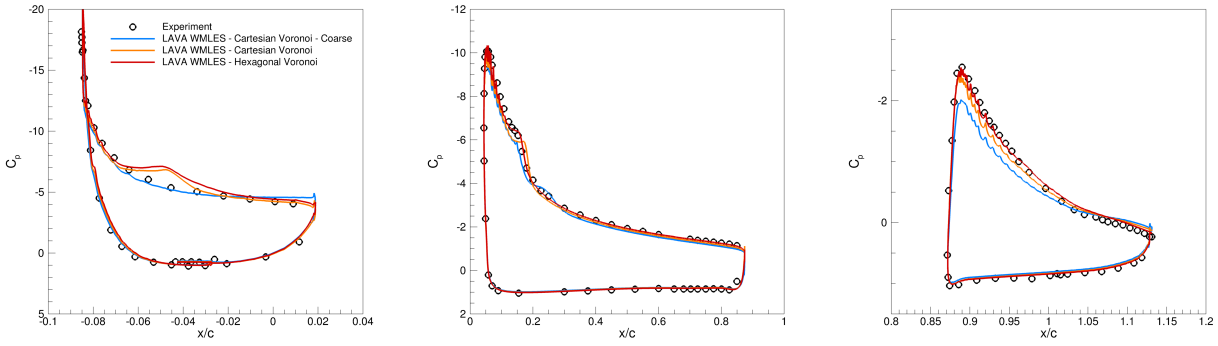

(c) $\alpha = 21.34°$

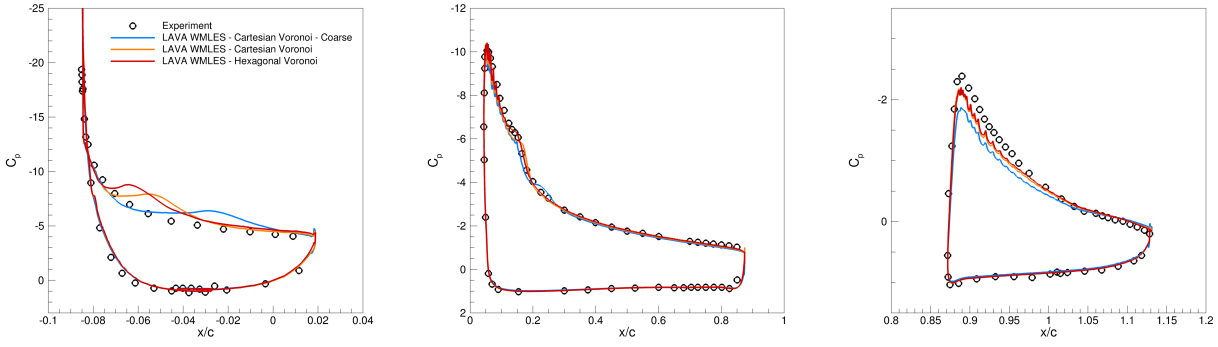

(d) $\alpha = 23.28°$

Fig. 16 Time-averaged pressure coefficient distributions over 30P30N slat (left), main (center) and flap (right) elements.

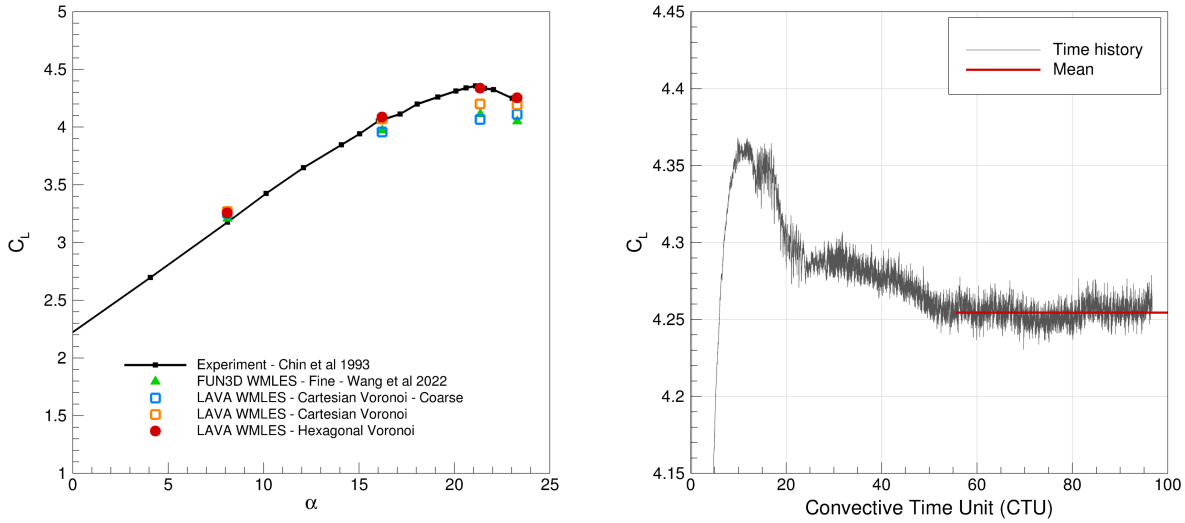

Fig. 17 Lift coefficient results for 30P30N. Right figure shows time history and the averaging interval for the LAVA WMLES - Hexagonal Voronoi case at $\alpha = 23.28°$.

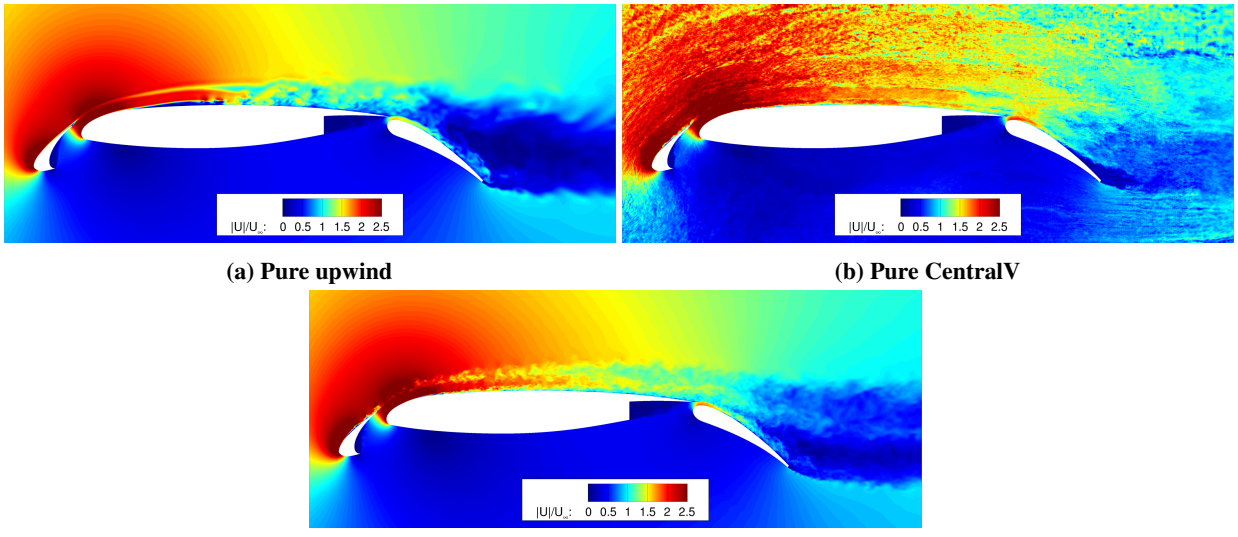

(a) Pure upwind

(b) Pure CentralV

(c) CentralV with upwind sensor

Fig. 18 Effect of the upwind sensor, showing instantaneous normalized velocity magnitude contours on the hexagonal prism mesh at $\alpha = 21.34$.

V. Conclusions

A 2nd order accurate cell-centered finite volume unstructured scheme suitable for large eddy simulations has been presented and tested with model problems of increasing complexity.

By studying isentropic vortex propagation through various Voronoi mesh types, we observed: (a) The convective scheme utilized is non-dissipative in uniform mesh regions of both cube (Cartesian seeding), truncated octahedron (BCC seeding) and rhombic dodecahedron (FCC seeding) cell types. (b) For a given mesh spacing, vortex dispersion errors are greatest for Cartesian mesh type, followed by BCC and FCC seeded meshes. (c) The subgrid scale model was sufficient to stabilize the scheme in existence of mesh size transitions. (d) Lloyd smoothing procedure at the coarse/fine interfaces helps reduce the error, although the effect was marginal for the vortex problem.

Forced Homogeneous Isotropic Turbulence (HIT) test also demonstrated the non-dissipative character of the convective flux discretization and verified the chosen subgrid scale model's utility in providing non-linear robustness as well as accuracy in representing the correct behavior for the turbulent energy cascade.

With the 30P30N multi-element airfoil case at a high Reynolds Number of 9×10^6, we verified the suitability of the proposed numerical scheme, along with Voronoi meshing approaches, to high-lift aerodynamics. The hexagonal prism Voronoi mesh simulation results were in overall excellent agreement with the experiment, both in terms of $C_{L,max}$ and the C_p distributions along each element. The only noticeable deviation from the experiment was observed over the slat upper surface where LES seems to predict a delayed transition to turbulence in comparison to the expected behavior that can be interpreted from the experimental C_p distributions. The Cartesian seeded mesh type resulted in an under-prediction of the $C_{L,max}$, despite having mesh sizing regions identical to the hexagonal prism mesh. However, the results with the Cartesian mesh displayed the correct trend of convergence with mesh refinement, leading us to the conclusion that for the same mesh spacing, the hexagonal mesh had a higher effective resolution.

VI. Acknowledgements

This work is funded by the NASA's Aeronautics Research Mission Directorate (ARMD) Transformational Tools and Technologies (T^3) project. Computing resources were provided by the NASA High-End Computing (HEC) Program's NASA Advanced Supercomputing (NAS) facility at Ames Research Center. We would like to thank the members of the LAVA Voronoi development team; Dr. Mahesh Natarajan (NASA Ames), Abram Rodgers (NASA Ames) and Keshav Sriram (NASA Ames). Their invaluable efforts in building the meshing tool enabled this work. We would also like to thank Dr. Gerrit Stich (NASA Ames) and Dr. Oliver Browne (NASA Ames) for their review and helpful feedback.

References

[1] Goc, K. A., Lehmkuhl, O., Park, G. I., Bose, S. T., and Moin, P., "Large eddy simulation of aircraft at affordable cost: a milestone in computational fluid dynamics," *Flow*, Vol. 1, 2021.

[2] Ghate, A. S., Stich, G.-D., Kenway, G. K., Housman, J. A., and Kiris, C. C., "A Wall-Modeled LES Perspective for the High Lift Common Research Model Using LAVA," *AIAA Aviation 2022 Forum*, 2022, p. 3434.

[3] Konig, B., Duda, B. M., and Laskowski, G. M., "Lattice Boltzmann Simulations for the 4th AIAA High-Lift Prediction Workshop using PowerFLOW," *AIAA AVIATION 2022 Forum*, 2022, p. 3433.

[4] Ahmad, N. N., Wang, L., Anderson, W. K., Balakumar, P., Iyer, P. S., and Nielsen, E. J., "FUN3D Simulations for the 4th AIAA High-Lift Prediction Workshop," , 2022.

[5] Browne, O. M., Housman, J. A., Kenway, G. K., Ghate, A. S., and Kiris, C. C., "A Hybrid RANS-LES Perspective for the High Lift Common Research Model Using LAVA," *AIAA AVIATION 2022 Forum*, 2022, p. 3523.

[6] Kiris, C. C., Ghate, A. S., Duensing, J. C., Browne, O. M., Housman, J. A., Stich, G.-D., Kenway, G., Dos Santos Fernandes, L. M., and Machado, L. M., "High-Lift Common Research Model: RANS, HRLES, and WMLES perspectives for CLmax prediction using LAVA," *AIAA SciTech 2022 Forum,* AIAA Paper 2022-1554, 2022. https://doi.org/10.2514/6.2022-1554.

[7] Ghate, A. S., Kenway, G. K., Stich, G.-D., Browne, O. M., Housman, J. A., and Kiris, C. C., "Transonic lift and drag predictions using wall-modelled large eddy simulations," *AIAA SciTech 2021 Forum,* AIAA Paper 2021-1439, 2021. https://doi.org/10.2514/6.2021-1439.

[8] Iyer, P. S., and Malik, M. R., "Wall-modeled LES of the NASA juncture flow experiment," *AIAA SciTech 2020 Forum,* AIAA Paper 2020-1307, 2020. https://doi.org/10.2514/6.2020-1307.

[9] Lozano-Duran, A., Bose, S. T., and Moin, P., "Prediction of trailing edge separation on the NASA Juncture Flow using wall-modeled LES," *AIAA SciTech 2020 Forum,* AIAA Paper 2020-1776, 2020. https://doi.org/10.2514/6.2020-1776.

[10] Ghate, A. S., Housman, J. A., Stich, G.-D., Kenway, G., and Kiris, C. C., "Scale resolving simulations of the NASA Juncture Flow Model using the LAVA solver," *AIAA Aviation 2020 Forum,* AIAA Paper 2020-2735, 2020. https://doi.org/10.2514/6.2020-2735.

[11] Rumsey, C., "4th AIAA High Lift Prediciton Workshop," , 2021. URL https://hiliftpw.larc.nasa.gov/.

[12] Kiris, C. C., Ghate, A. S., Browne, O. M., Slotnick, J. P., and Larsson, J., "HLPW-4/GMGW-3: Wall-Modeled LES and Lattice-Boltzmann Technology Focus Group Workshop Summary," *AIAA AVIATION 2022 Forum*, 2022, p. 3294.

[13] Larsson, J., Kawai, S., Bodart, J., and Bermejo-Moreno, I., "Large eddy simulation with modeled wall-stress: recent progress and future directions," *Mechanical Engineering Reviews*, Vol. 3, No. 1, 2016, pp. 15–00418.

[14] Park, G. I., "Wall-modeled large-eddy simulation of a high Reynolds number separating and reattaching flow," *AIAA Journal*, Vol. 55, No. 11, 2017, pp. 3709–3721.

[15] Ghate, A., and Lele, S. K., "Finite difference methods for turbulence simulations," *Numerical Methods in Turbulence Simulation*, 2022, p. 235.

[16] Trefethen, L. N., "Group velocity in finite difference schemes," *SIAM review*, Vol. 24, No. 2, 1982, pp. 113–136.

[17] Sescu, A., Hixon, R., and Afjeh, A. A., "Multidimensional optimization of finite difference schemes for computational aeroacoustics," *Journal of Computational Physics*, Vol. 227, No. 9, 2008, pp. 4563–4588.

[18] Hamilton, B., and Bilbao, S., "Hexagonal vs. rectilinear grids for explicit finite difference schemes for the two-dimensional wave equation," *Proceedings of Meetings on Acoustics ICA2013*, Vol. 19, Acoustical Society of America, 2013, p. 015120.

[19] Bres, G. A., Bose, S. T., Emory, M., Ham, F. E., Schmidt, O. T., Rigas, G., and Colonius, T., "Large-eddy simulations of co-annular turbulent jet using a Voronoi-based mesh generation framework," *2018 AIAA/CEAS Aeroacoustics Conference*, 2018, p. 3302.

[20] Bose, S., Wang, K., Ivey, C., and Ham, F., "Tractability of LES for complex flows," *APS Division of Fluid Dynamics Meeting Abstracts*, 2019, pp. H16–002.

[21] Vichnevetsky, R., "Wave propagation and reflection in irregular grids for hyperbolic equations," *Applied numerical mathematics*, Vol. 3, 1987, pp. 133–166.

[22] Yalla, G. R., Oliver, T. A., Haering, S. W., Engquist, B., and Moser, R. D., "Effects of resolution inhomogeneity in large-eddy simulation," *Physical Review Fluids*, Vol. 6, No. 7, 2021, p. 074604.

[23] Stich, G.-D., Ghate, A. S., Housman, J. A., and Kiris, C. C., "Wall-Modeled Large-Eddy Simulation of Jet Noise in Flight Conditions," *28th AIAA/CEAS Aeroacoustics 2022 Conference*, 2022, p. 3002.

[24] Wong, M. L., Kenway, G. K., Ghate, A. S., Stich, G.-D., and Kiris, C. C., "Predictions of LAGOON Nose Landing Gear Flow and Noise using Wall-Modeled Large-Eddy Simulations," *28th AIAA/CEAS Aeroacoustics Conference*, 2022.

[25] Lloyd, S., "Least squares quantization in PCM," *IEEE Transactions on Information Theory*, Vol. 28, No. 2, 1982, pp. 129–137. https://doi.org/10.1109/TIT.1982.1056489.

[26] Kiris, C. C., Barad, M. F., Housman, J. A., Sozer, E., Brehm, C., and Moini-Yekta, S., "The LAVA computational fluid dynamics solver," *52nd Aerospace Sciences Meeting*, 2014, p. 0070.

[27] van Leer, B., "Towards the Ultimate Conservative Difference Scheme. II. Monotonicity and Conservation Combined in a Second-order Scheme," *Journal of Computational Physics*, Vol. 14, 1974, pp. 361–370. https://doi.org/10.1016/0021-9991(74)90019-9.

[28] Sozer, E., Brehm, C., and Kiris, C. C., "Gradient Calculation Methods on Arbitrary Polyhedral Unstructured Meshes for Cell-Centered CFD Solvers," *52nd Aerospace Sciences Meeting*, 2014. https://doi.org/10.2514/6.2014-1440, URL https://arc.aiaa.org/doi/abs/10.2514/6.2014-1440.

[29] Roe, P. L., "Characteristic-Based Schemes for the Euler Equations," *Annual Review of Fluid Mechanics*, Vol. 18, No. 1, 1986, pp. 337–365. https://doi.org/10.1146/annurev.fl.18.010186.002005, URL https://doi.org/10.1146/annurev.fl.18.010186.002005.

[30] Kim, K. H., Kim, C., and Rho, O.-H., "Methods for the Accurate Computations of Hypersonic Flows: I. AUSMPW+Scheme," *Journal of Computational Physics*, Vol. 174, No. 1, 2001, pp. 38–80. https://doi.org/https://doi.org/10.1006/jcph.2001.6873, URL https://www.sciencedirect.com/science/article/pii/S0021999101968731.

[31] Mittal, R., and Moin, P., "Suitability of upwind-biased finite difference schemes for large-eddy simulation of turbulent flows," *AIAA Journal*, Vol. 35, No. 8, 1997, pp. 1415–1417.

[32] Jalali, A., Sharbatdar, M., and Ollivier-Gooch, C., "Accuracy analysis of unstructured finite volume discretization schemes for diffusive fluxes," *Computers & Fluids*, Vol. 101, 2014, pp. 220–232. https://doi.org/https://doi.org/10.1016/j.compfluid.2014.06.008, URL https://www.sciencedirect.com/science/article/pii/S0045793014002473.

[33] Vreman, A., "An eddy-viscosity subgrid-scale model for turbulent shear flow: Algebraic theory and applications," *Physics of Fluids*, Vol. 16, No. 10, 2004, pp. 3670–3681.

[34] Musker, A. J., "Explicit Expression for the Smooth Wall Velocity Distribution in a Turbulent Boundary Layer," *AIAA Journal*, Vol. 17, No. 6, 1979, pp. 655–657. https://doi.org/10.2514/3.61193, URL https://doi.org/10.2514/3.61193.

[35] Gottlieb, S., Shu, C.-W., and Tadmor, E., "Strong Stability-Preserving High-Order Time Discretization Methods," *SIAM Review*, Vol. 43, No. 1, 2001, pp. 89–112. https://doi.org/10.2307/3649684, URL http://www.jstor.org/stable/3649684.

[36] Rizzi, A. W., and Inouye, M., "Time-Split Finite-Volume Method for Three-Dimensional Blunt-Body Flow," *AIAA Journal*, Vol. 11, No. 11, 1973, pp. 1478–1485. https://doi.org/10.2514/3.50614, URL https://doi.org/10.2514/3.50614.

[37] Hu, F. Q., Li, X. D., and Lin, D., "Effects of the computational time step on numerical solutions of turbulent flow," *Journal of Computational Physics*, Vol. 227, No. 9, 2008, pp. 4398–4424. https://doi.org/10.1016/j.jcp.2008.01.010.

[38] Carton de Wiart, C., Hillewaert, K., Duponcheel, M., and Winckelmans, G., "Assessment of a discontinuous Galerkin method for the simulation of vortical flows at high Reynolds number," *International Journal for Numerical Methods in Fluids*, Vol. 74, 2014, p. 469–493. https://doi.org/10.1002/fld.3859.

[39] Rosales, C., and Meneveau, C., "Linear forcing in numerical simulations of isotropic turbulence: Physical space implementations and convergence properties," *Physics of fluids*, Vol. 17, No. 9, 2005, p. 095106.

[40] Chin, V., Peters, D., Spaid, F., and McGhee, R., "Flowfield measurements about a multi-element airfoil at high Reynolds numbers," *23rd Fluid Dynamics, Plasmadynamics, and Lasers Conference*, 1993. https://doi.org/10.2514/6.1993-3137, URL https://arc.aiaa.org/doi/abs/10.2514/6.1993-3137.

[41] Bodart, J., Larsson, J., and Moin, P., "Large eddy simulation of high-lift devices," *21st AIAA Computational Fluid Dynamics Conference*, 2013. https://doi.org/10.2514/6.2013-2724, URL https://arc.aiaa.org/doi/abs/10.2514/6.2013-2724.

[42] Angelino, M., Fernández-Yáñez, P., Xia, H., and Page, G. J., "Large-Eddy Simulation with Modeled Wall Stress for Complex Aerodynamics and Stall Prediction," *AIAA Journal*, Vol. 59, No. 4, 2021, pp. 1225–1237. https://doi.org/10.2514/1.J059481, URL https://doi.org/10.2514/1.J059481.

[43] Klausmeyer, S., and Lin, J., "Comparative Results from A CFD Challenge Over a 2D Three-Element High-Lift Airfoil," *NASA/TM-112858*, 1997.

[44] Wang, L., Anderson, W. K., Nielsen, E. J., Balakumar, P., Park, M. A., Carlson, J.-R., Iyer, P. S., and Diskin, B., "Wall-Modeled Large-Eddy Simulations for High-Lift Configurations using FUN3D (Invited)," *AIAA SciTech 2022 Forum*, 2022. https://doi.org/10.2514/6.2022-1555, URL https://arc.aiaa.org/doi/abs/10.2514/6.2022-1555.